Petroleum Science 19 (2022) 2268–2283

Contents lists available at ScienceDirect

Petroleum Science

journal homepage: www.keaipublishing.com/en/journals/petroleum-science

Original Paper

Numerical simulation on proppant migration and placement within the rough and complex fractures

Tian-Kui Guo [a, *], Zhi-Lin Luo [b], Jin Zhou [c], Yuan-Zhi Gong [d], Cai-Li Dai [a], Jin Tang [e], Yang Yu [f], Bing Xiao [f], Bao-Lun Niu [g], Ji-Jiang Ge [a]

[a] College of Petroleum Engineering, China University of Petroleum (Huadong), Qingdao, 266580, Shandong, China
[b] Southwest Oil and Gas Field Company, PetroChina, Chengdu, 610051, Sichuan, China
[c] Exploration Division, Tarim Oilfield Company, PetroChina, Korla, 841000, Xinjiang, China
[d] Dongxin Oil Production Plant, Shengli Oil Field Branch, Sinopec, Dongying, 257100, Shandong, China
[e] Research Institute of Petroleum Exploration and Development, PetroChina, Beijing, 100083, China
[f] Zhongyuan Petroleum Engineering Company, Sinopec, Puyang, 457001, Henan, China
[g] Zhongyuan Oilfield Company, Sinopec, Puyang, 457001, Henan, China

ARTICLE INFO

Article history:
Received 18 October 2021
Received in revised form
31 March 2022
Accepted 13 April 2022
Available online 18 April 2022

Edited by Yan-Hua Sun

Keywords:
Hydraulic fracturing
Proppant migration and placement
Rough fracture wall
Complex fracture
CFD-DEM coupling

ABSTRACT

Hydraulic fracturing is a key technology for the development of unconventional hydrocarbon resources. The proppant placement morphology determines the fracture conductivity, thus affecting the reservoir stimulation effect. In this paper, the proppant migration and placement within complex fractures was studied by considering the fracture wall roughness through computational fluid mechanics-discrete element method (CFD-DEM) in numerical simulation, which is a key approach to study the proppant migration and placement. The results show that the proppant placement non-uniformity, proppant migration capacity, and proppant volume filled in the far-end and the secondary branched fracture are enhanced within the rough fracture compared with those within smooth fractures. The proppant migration capacity is increased within the fracture at low inclination angles (<60°) and low approach angles (<90°), and the proppant placement area is larger in the inclined fracture than that in the vertical fracture. The rise of injection rate and fracturing fluid viscosity causes more proppants migrate to far-end or secondary fractures, resulting in a non-proppant area within the near-wellbore fracture. An increase by 1.3 times in the injection rate and 3 times in the fracturing fluid viscosity leads to a decrease by 26.6% and 27%, respectively, in the proppant placement area within the near-wellbore fracture. The staged injection with small size proppants followed by large size proppants increases the proppant placement area in the primary fracture by 13%–26%, and that with large size proppants followed by small size proppants increases the proppant placement area by 19%–25%, which is due to that the latter method facilitates filling of the secondary branched fracture. The injection location mainly affects the proppant filling degree within the near-wellbore fractures. Compared with the upper injection, the middle and lower injection is not beneficial to filling of proppants within the near-wellbore fracture.

1. Introduction

The development of unconventional hydrocarbon is increasing due to the depletion of conventional hydrocarbon resources. Hydraulic fracturing is a requisite and plays a key role in developing unconventional hydrocarbon reservoirs (Sahai and Moghanloo, 2019; Liu et al., 2019; Abubakar et al., 2021). The created fractures are gradually closed after hydraulic fracturing operation due to the existence of *in-situ* stress. The proppants are carried by the carrier fluids and injected into the reservoir during hydraulic fracturing to prevent fracture closure (Beatriz et al., 2021; Ainni et al., 2021) and maintain the high conductivity of proppant-propped fractures, which are the high-rate channels for oil and gas flow to the wellbore (Guo et al., 2017; Gong et al., 2020). The proppant migration and placement morphology directly determine the conductivity of the proppant-filled fracture. It is necessary to investigate the

* Corresponding author.
E-mail address: guotiankui@126.com (T.-K. Guo).

https://doi.org/10.1016/j.petsci.2022.04.010

influences of relevant factors on proppant migration and placement and understand the laws of proppant migration and placement in fracturing design.

Physical simulation is a key approach in study of proppant migration and placement. Bandara et al. (2020) made some progress in the study of the mechanism of proppant migration, distribution, crushing and embedment within fractures in real cores with a diameter of only 5 cm. Studies have been done previously in large outcrop rocks (Guo et al., 2020), but the cost in outcrop rock excavation, acquirement, cutting, migration and experimental operation is quite high. Currently, the laboratory experiment is completed in the simulation devices of proppant migration and placement. The simulation devices with different characteristics have been built by Sahai et al. (2014), Raimbay et al. (2017), Alotaibi and Miskimins (2017), Ba et al. (2019), and Troy et al. (2020), and the study of proppant migration and placement has been completed. The physical simulation provides visual observation of proppant migration and placement and reliable results, but it is not applicable in fracturing design due to the fixed structure and single boundary conditions of the simulation devices.

With the progress of the computer technology, numerical simulation has become another method in the study of proppant migration and placement (Guo et al., 2019; Gong et al., 2016). Comparatively, numerical simulation is more helpful in fracturing design due to low cost, various model forms and various boundary conditions. Currently, numerical simulation of fluid-particle two-phase flow are completed through Euler-Euler and Euler-Lagrang methods (Gadde et al., 2004). In computational fluid dynamics (CFD), which is a Euler-Euler method, the fluid and the particle phases are as a continuum and a pseudo fluid respectively, and the dynamical characteristics of the particle phase are similar to those of the fluid phase. Tsai et al. (2012) used the CFD method to carry out numerical simulation of proppant migration within hydraulic fractures in shale gas reservoirs, and the fracture geometry was simplified ensure good performance of model computing. Bokane et al. (2013) used the CFD method to study the proppant migration and distribution in multi-stage fractured horizontal wells, and analyzed the effects of fracturing fluid viscosity, injection rate and proppant particle size. Gong et al. (2020) carried out the study of proppant migration within natural and secondary fractures with the CFD method. The results show that the secondary fracture direction controls the proppant migration efficiency and motion morphology and directly determines the proppant placement within the secondary fracture.

In computational fluid dynamics-discrete element method (CFD-DEM) coupling, which is a Euler- Lagrang method, the fluid migration equation in the Lagrange coordinate system is resolved by considering the fluid as continuous phase, and the particle motion equation is solved in the Lagrange coordinate system by considering the particle phase as a finite discrete element. Zhang et al. (2017) studied the effects of proppant particle size, density, fracturing fluid viscosity and injection rate on proppant migration and placement within a single fracture across horizontal wells through numerical simulation with the CFD-DEM coupling method. The result shows that proppant motion is mainly affected by the fluid dynamics of fracturing fluid. Proppants start to settle near the wellbore, and they are balanced as more proppants settle down. Then, the proppants injected subsequently migrated to the far end of the fracture. Kou et al. (2018) carried out simulation of proppant migration and settlement in a single inclined fracture through CFD-DEM, and the result shows that proppant placement in inclined fractures is better than that in vertical fractures due to the fracture wall supporting force. Wang et al. (2019) analyzed the effects of fracture closure, perforation height and secondary fracture approach angle by simulation of proppant migration and placement within smooth and complex fractures through CFD-DEM. The results show that fracture closure leads to an increase in the placement area and a reduction in the proppant layer. The perforation height has an effect on mixing of multi-size proppants. Proppants are more easily migrated to the branched fractures of larger entrance and smaller approach angle. Lu et al. (2020) obtained the reason and mechanism of uneven proppant placement and low propping efficiency within a single simplified fracture through CFD-DEM simulation with variable fracturing fluid viscosity and proppant density. The study shows that an increase in the fluid viscosity leads to a significant increase in the proppant migration distance and an increase in the non-proppant length near the wellbore. The best fracture propping effect is obtained through alternated injection of the fracturing fluids with the viscosity ratio between 2 and 5. High density proppants can be deposited to form a higher proppant bed, and lower density proppants tend to form a longer proppant bed. Song and Dahi (2020) performed the CFD-DEM numerical simulation of proppant migration and placement within smooth and symmetrical complex fractures. The result shows that the injected proppants are divided into bottom sand dune zone, middle rolling zone and top fluidized zone. The balanced height of the sand dune within the secondary fractures is possibly higher than that within the primary fracture, and the proppant sand dunes are symmetrically distributed. Proppants settle down through falling deposition and rolling deposition within secondary fractures. In addition, the MP-PIC method, which also belongs to the Eulerian-Lagrangian model, is also used in the study of proppant migration and placement. This method is different from CFD-DEM in that it divides the dispersed phase into many small parts. Then, instead of calculating each proppant particle, each small part of the particle is packaged as the simulation calculation object to reduce the computational cost. Siddhamshetty et al. (2020) used a computationally efficient, three-dimensional, multiphase particle-in-cell (MP-PIC) model was employed to simulate the multi-size proppant transport in a field-scale geometry using the Eulerian–Lagrangian framework. Zeng et al. (2019) studied the transport of proppant in large-scale extended fractures based on the MP-PIC method, providing new insights for field-scale simulations.

Numerical simulation is a powerful tool to study proppant migration and placement. Particularly, the CFD-DEM coupling method is widely used due to its capability of capturing the particle motion characteristics and accurately characterizing the interaction between particles, fluid and fracture wall surface. Previously, the fracture model was simplified as the smooth fracture wall, where the effect of the rough fracture wall on proppant migration and placement is always neglected. Moreover, the fracture model is mostly treated as the single primary fracture, and there is no research on proppant migration within complex fractures of different morphology. In this paper, numerical simulation of proppant migration and placement within the complex rough fracture was performed through CFD-DEM coupling method to obtain the influencing mechanism of the fracture characteristics, including the fracture wall roughness and the inclined angle and approach angle of secondary fracture and the operation parameters, including the injection rate, proppant particle size and fracturing fluid viscosity and injection location, and the suggestions on field fracturing were given.

2. Simulation methods

In CFD, solution of the governing equations of fluid mechanics and simulation of the hydrodynamic problems are realized by the numerical method. In DEM, tracking of individual particle motion and simulation of interaction between particles can be realized. The

CFD-DEM coupling method can be used to simulate proppant migration and placement within the rough fractures, and fluid flow and particle motion are computed in CFD and DEM solvers, respectively. The CFD-DEM coupling processes (Zeng et al., 2016) are as follows: compute the fluid flow through CFD in each time step, transfer the fluid flow to DEM via pressure and momentum, compute location and velocity of updated particles, return the updated data to CFD, update the fluid pressure and velocity field, and continue computation in the next time step, as shown in Fig. 1.

(1) Incompressible fluid governing equation (Zeng et al., 2016; Zhang et al., 2017; Wang et al., 2019)

$$\frac{\partial}{\partial t}\left(\alpha_f \rho_f\right) + \nabla \cdot \left(\alpha_f \rho_f \boldsymbol{u}_f\right) = 0 \tag{1}$$

$$\frac{\partial}{\partial t}\left(\alpha_f \rho_f \boldsymbol{u}_f\right) + \nabla \cdot \left(\alpha_f \rho_f \boldsymbol{u}_f \boldsymbol{u}_f\right) = -\nabla \boldsymbol{P} + \nabla \cdot \left(\alpha_f \boldsymbol{\tau}_f\right) + \alpha_f \rho_f \boldsymbol{g} - \boldsymbol{F}_f^{pf} \tag{2}$$

$$\boldsymbol{F}_f^{pf} = \alpha_f \rho_f \left(\boldsymbol{F}_f + \boldsymbol{F}_{lift} + \boldsymbol{F}_{vm}\right) \tag{3}$$

where α_f is the volume fraction of fluid; ρ_f is the fluid density; $\boldsymbol{u}_f$ is the fluid velocity; $\boldsymbol{\tau}_f$ is the viscous stress tensor; $\boldsymbol{P}$ is the fluid pressure; $\boldsymbol{g}$ is the acceleration of gravity; $\boldsymbol{F}_f^{pf}$ is the external force on the element fluid; $\boldsymbol{F}_f$ is the volume force; $\boldsymbol{F}_{lift}$ is the lift force; $\boldsymbol{F}_{vm}$ is the virtual mass force.

(2) Particle governing equation (Wang et al., 2019)

The governing equations of particle translation and rotation are shown in Eqs. (4) and (5). The normal and tangential interactions between particles are characterized in Eq. (6).

$$m_p \frac{d\boldsymbol{v}_p}{dt} = \boldsymbol{F}_p^c + m_p \boldsymbol{g} + \boldsymbol{F}_p^{fp} \tag{4}$$

$$\boldsymbol{I}_p \frac{d\boldsymbol{\omega}_p}{dt} = \sum \boldsymbol{T} \tag{5}$$

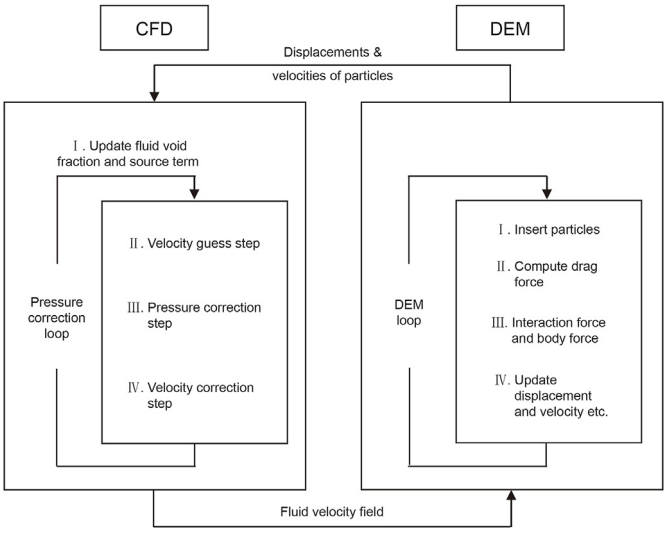

Fig. 1. CDF-DEM coupling process (Reprint permission obtained from Zeng et al., 2016).

$$\boldsymbol{F}_p^c = \left(\boldsymbol{F}_n n - \boldsymbol{F}_n^d n\right) + \left(\boldsymbol{F}_t t - \boldsymbol{F}_t^d t\right) \tag{6}$$

where $\boldsymbol{F}_p^c$ is the contact force; $\boldsymbol{F}_p^{fp}$ is the fluid drag force and pressure gradient force on particles; m_p is the particle mass; $\boldsymbol{I}_p$ is the moment of inertia of particles; $\boldsymbol{n}$ is the normal direction between particles; $\sum \boldsymbol{T}$ is the sum of torque vectors on particles; $\boldsymbol{v}_p$ is the particle velocity; ω_p is the angular velocity of particles.

(3) CFD-DEM coupling (Wang et al., 2019)

Pressure gradient force:

$$\boldsymbol{F}_{\nabla P} = -\boldsymbol{V}_p \nabla \boldsymbol{P} \tag{7}$$

Fluid drag force:

$$\boldsymbol{F}_D = \beta(\boldsymbol{u} - \boldsymbol{v}) \tag{8}$$

where $\boldsymbol{V}_p$ is the proppant volume; β is the dimensionless coefficient calculated by Wen & Yu's method (Wen and Yu, 1966).

$$\beta = 150\frac{\left(1-\alpha_f\right)^2}{\alpha_f}\frac{\mu}{d_p^2} + 1.75\left(1-\alpha_f\right)\frac{\rho}{d_p}\left|(\boldsymbol{u}-\boldsymbol{u}_p)\right| \quad \text{when } \alpha_f < 0.8 \tag{9}$$

$$\beta = 0.75\frac{C_d}{d_p} + \rho\left(1-\alpha_f\right)\alpha_f^{-2.7}\left|(\boldsymbol{u}-\boldsymbol{u}_p)\right| \quad \text{when } \alpha_f \geq 0.8 \tag{10}$$

$$\boldsymbol{F}_D = \frac{V_p \beta}{\left(1-\alpha_f\right)}(\boldsymbol{u}-\boldsymbol{u}_p) \tag{11}$$

where d_p is the particle diameter; $\boldsymbol{u}$ is the fluid velocity; $\boldsymbol{u}_p$ is the particle velocity; C_d is the drag coefficient, which is defined by the particle Reynolds number.

$$C_d = \frac{24\left(1 + 0.15 Re_p^{0.687}\right)}{Re_p}, \quad Re_p \leq 1000 \tag{12}$$

$$C_d = 0.44, \quad Re_p > 1000 \tag{13}$$

3. Establishment of rough fracture model

Currently, the study of proppant placement and migration within the fractures is always carried out with the smooth and simplified models. Nevertheless, the actual inner wall of fracture is rough and uneven. More needs to be done in the study of the mechanism of rough wall affecting proppant migration. Steven et al. (2006) proposed a method for creating the numerical rough rock fracture wall and developed the supporting software package SynFrac, which are used to generate a series of altitude data of fracture wall of different roughness. In this method, several parameters are input to control the spatial correlation of rough fracture surfaces and the correlation between fracture surfaces. The fracture wall roughness is characterized by fractal dimension (D_f), and the higher fractal dimension indicates the rougher fracture wall. Scott et al. (2016) confirmed the validity of this method by numerical simulation of the effect of roughness on fluid flow and eddy forming within a series of numerical fracture models of increasing roughness generated in SynFrac and comparing the

numeric results with the experimental results. Yatin et al. (2019) used this method to create a series of numerical fracture models of different roughness and carried out study of proppant migration in the fracture using CFD method, and the reliability of the method was proved. In this paper, we only consider the effect of rough sidewall of the fracture on proppant migration, ignore the morphology of the fracture top and bottom, and do not consider the phenomenon that the fracture will close under *in-situ* stress. First, use SynFrac to generate the elevation data of the rough fracture on both sides of the fractal dimension value, import the rough wall data on one side into the modeling software (Solidworks is used in this paper), then use the "boundary surface" function of Solidworks to generate one side. In the same way, the rough fracture surface on the other side is generated, and the distance between the two side walls is adjusted according to the simulated fracture width requirements (because both side walls have bumps of different sizes, the average distance between the two sides is taken as the fracture width in this paper.), then sew the edges around the two side walls into four smooth surfaces, which are the top surface, bottom surface, entrance surface, and exit surface of the fracture, and finally generate a single-block 3D rough fracture model with a certain width (as shown in Fig. 2). Using a single three-dimensional rough fracture model as a "building block" to "build building blocks", complex rough fracture models with different shapes can be obtained. Babadagli and Develi (2003) found the fractal dimension of fracture wall from 2 to 2.7 in rock fracturing in the laboratory. In this paper, the fracture wall roughness is set as $D_f = 2$ (smooth fracture), $D_f = 2.3$ and $D_f = 2.7$, and the length × height × width of the primary fracture is 500 mm × 60 mm × 5 mm, and that of the secondary fracture is 150 mm × 60 mm × 3 mm.

4. Verification of numerical simulation method

The numerical simulation results were compared with those of previous experiments in the smooth fracture to verify the accuracy of the method and were compared with those of laboratory experiments in rough fractures to verify the reliability of proppant migration and placement rules within rough fractures.

4.1. Comparison with experiments in the smooth fracture

In order to verify the accuracy of the numerical simulation method, the same parameters and a similar fracture model were used for simulation, which was compared with the experimental results of Tong and Mohanty (2016). Used parameters in the simulation are shown in Table 1, and the other parameters not listed are consistent with the experiments. It can be seen from Fig. 3 that the numerical simulation results are similar to the sand dune morphology in the experimental results. The number of proppants entering the branch fractures is limited. Now, we mainly compare and analyze the sand dune parameters in the main fractures, and

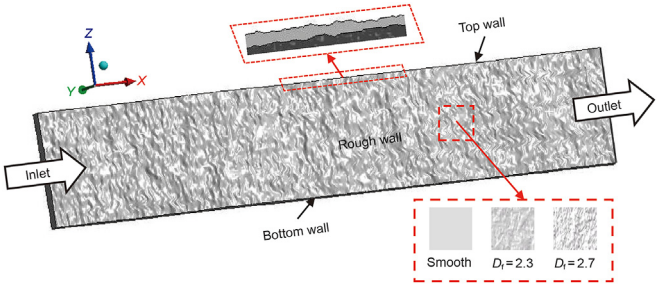

Fig. 2. 3D fracture model with the rough wall.

Table 1
Numerical simulation parameters.

Parameters	Value
Primary fracture size $L \times H \times W$, m	0.3810 × 0.0762 × 0.002
Branched fracture size $L \times H \times W$, m	0.1905 × 0.0762 × 0.002
Proppant size, mm	0.6 mm
Fracturing fluid density, kg/m^3	1000
Fracturing fluid viscosity, Pa s	0.001
Fluid injection rate, m/s	0.1, 0.2
Proppant density, kg/m^3	2650
Injection time, s	20

draw the sand dune parameter histograms under the two schemes of case 1 and case 2, as shown in Fig. 4. The errors in the length and average height of the sand dune between the simulation and experimental results of case 1 are 8.8% and 4.5%, respectively, while those of case 2 are 2.8% and 5.0%. The above data results show that the numerical simulation results are in good agreement with the experimental results, and the mathematical model can be used to study the law of proppant migration and placement in fractures.

4.2. Comparison with experiments in the rough fracture

Guo et al. (2018) developed a simulation device of proppant migration and placement within the large complex and rough fractures (Fig. 5a). The device consists of several fracture units with filtration holes (Fig. 5b), which can be installed independently or integrated to form a long fracture. One fracture wall is bonded with rock particles to form the roughness (Fig. 5b), and the other wall is the transparent organic glass. A single-wall rough fracture model (Fig. 5c) with the same size and similar roughness as the unit fracture in the simulation device was created in simulation calculation. The effect of fluid leaked off was not considered in this study, and the filtration holes were closed in the experiment. According to the parameter conditions in Table 2, two groups of laboratory experiments and numerical simulations were compared and verified. The results are shown in Fig. 6. The sand dune shapes of the experiment and the numerical simulation are similar under two schemes. Due to the limitation of the model size, the proppant migration distance has exceeded the fracture length, so it is not meaningful to compare the length of the sand dune, while ratio of dune area to fracture area can be very good to evaluate the effect of proppant propping and filling fractures, so a bar chart (Fig. 7) comparing average height and ratio of dune area to fracture area under the two schemes is drawn. The errors of the average height and ratio of dune area to fracture area between the simulation results and the experimental results in case 1 are 3.7% and 10.1%, respectively, while those in case 2 are 3.8% and 7.6%. The above errors are mainly caused by the roughness of the wall surface of the experimental device and the roughness of the digital fracture model, as well as the sealing degree and improper operation of the experimental device, but the error is within the acceptable range. Therefore, it can be judged that the numerical simulation of proppant migration and placement in rough wall fractures using CFD-DEM method is reliable and the results are reliable.

5. Results and analysis

5.1. Numerical simulation scheme

In this paper, numerical simulation of proppant migration and placement within the complex rough fracture was performed through CFD-DEM coupling method to obtain the influencing mechanism of the fracture characteristics, including the fracture

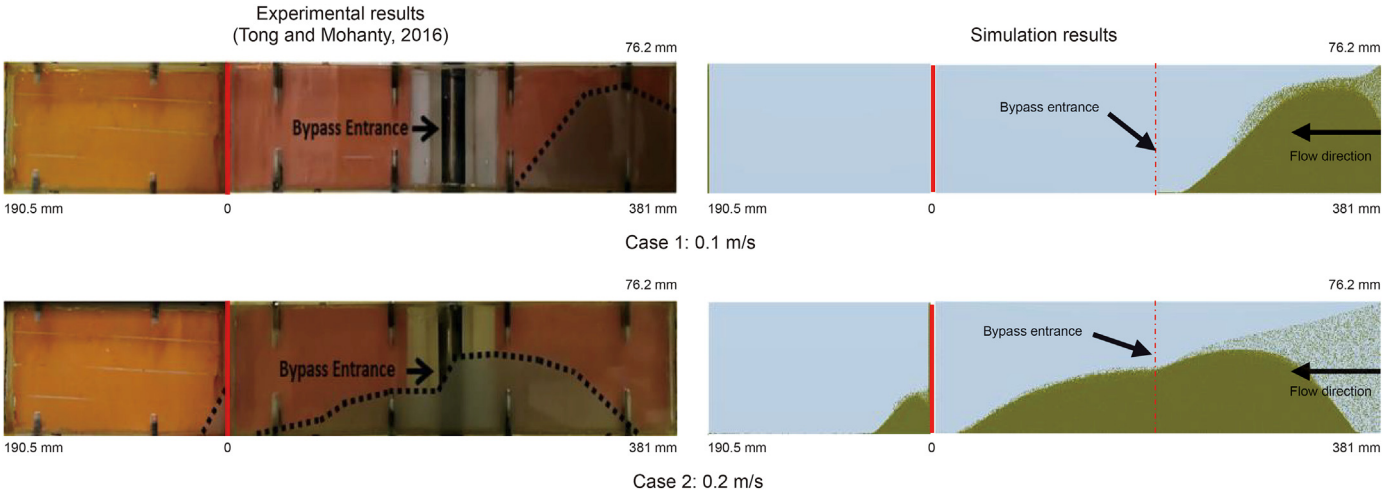

Fig. 3. Comparison of results of laboratory experiments (Reprint permission obtained from Tong and Mohanty, 2016) and numerical simulation in the smooth fracture.

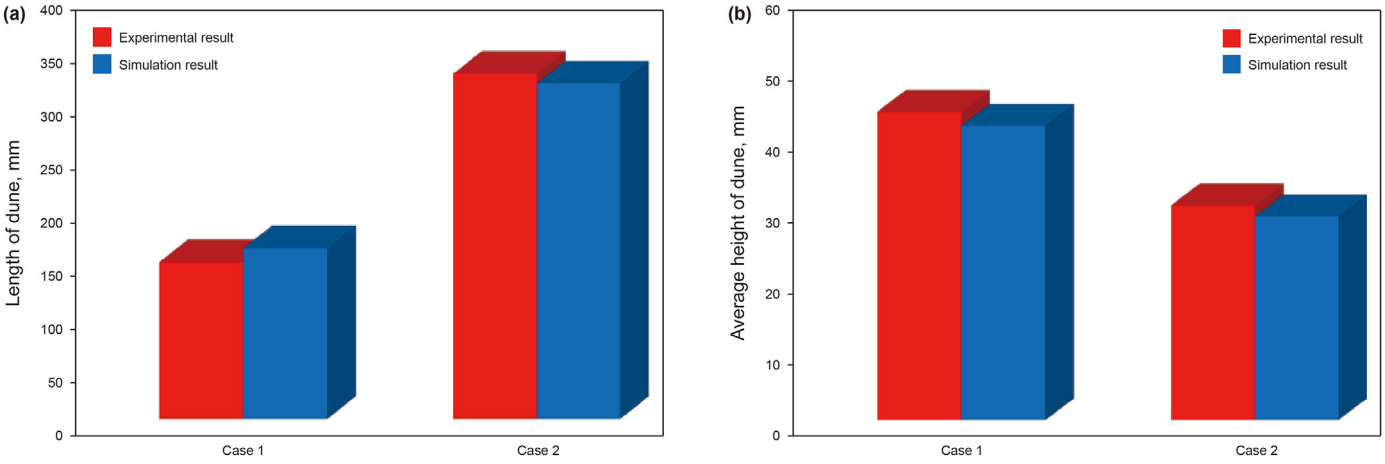

Fig. 4. Comparison of sand dune parameters between simulation results and experimental results in case 1 and case 2 in smooth fractures. (**a**) Length of sand dune; (**b**) Average height of sand dune.

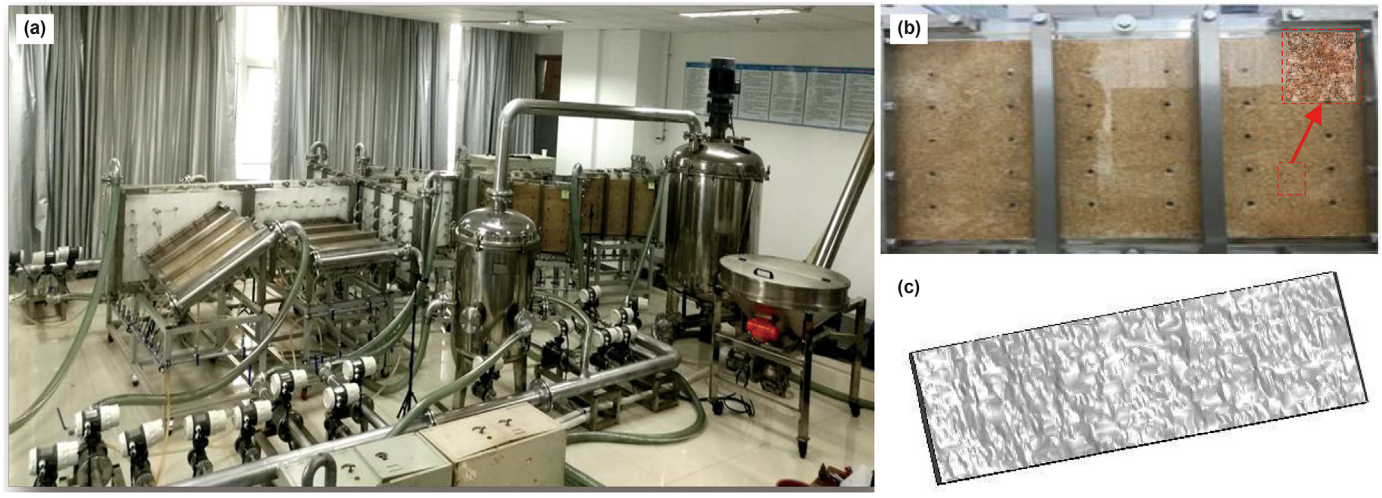

Fig. 5. (**a**) Proppant migration and placement simulation device for large complex fractures; (**b**) Single block rough fracture slot; (**c**) Unilateral rough wall fracture model.

Table 2
Parameters in experiments and numerical simulation.

Parameters	Value
Fracture size $L \times H \times W$, m	$1 \times 0.005 \times 0.6$
Inlet and outlet conditions	Full open
Fracturing fluid type in experiment	Slickwater
Fracturing fluid density in numerical simulation, kg/m^3	1000
Fracturing fluid viscosity in numerical simulation, Pa s	0.005
Fluid injection rate, m/s	0.5, 0.3
Proppant type in experiment	Quartz sand
Proppant density in numerical simulation, kg/m^3	2500
Proppant size in experiment, mesh	20/40, 40/70
Proppant size in numerical simulation, mm	0.6, 0.3
Proppant concentration, %	15

wall roughness and the inclined angle and approach angle of secondary fracture and the operation parameters, including the injection rate, proppant particle size and fracturing fluid viscosity and injection location. The simulation scheme is illustrated in Table 3.

The simulation was performed in a pressure-based solver by assuming gravity in the fracture height direction, selecting the k–ε turbulence model, and setting the inlet as the rate entrance boundary, the outlet as the pressure exit boundary, the fracture wall as the non-slipping wall boundary and the time step as 1×10^{-5} s and 1×10^{-3} s in DEM and CFD solvers, respectively. The proppant size was set as 0.8 mm, which is larger than the field proppant size. This is due to that a very small proppant diameter causes a significant increase in particle number under the fixed proppant concentration, leading to a large increase in the simulation time and failure in computation (Deng et al., 2014; Wu and Sharma, 2016). Mixing and pumping of proppants and fracturing fluid was simulated by setting the equal injection rate. Considering the complex wall characteristics of the rough fracture model, the model was meshed by the mixing network. The physical properties of the proppant and fluid and other parameters in the simulation are listed in Table 4.

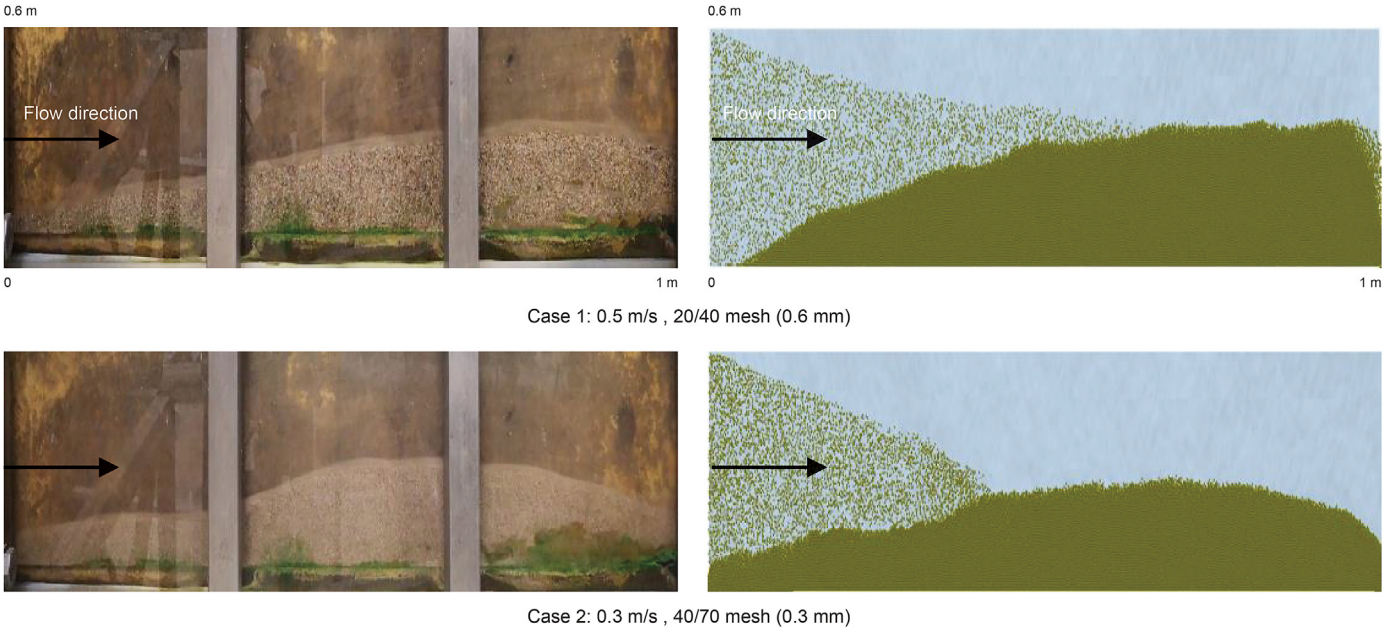

Fig. 6. Comparison of results of laboratory experiments and numerical simulation in the rough fracture.

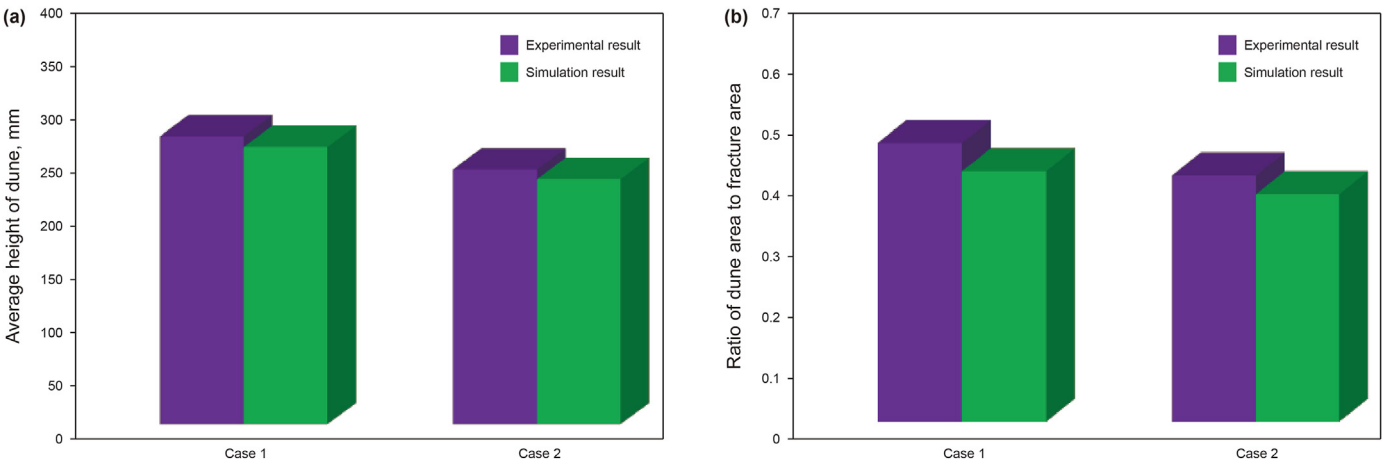

Fig. 7. Comparison of sand dune parameters between simulation results and experimental results under two schemes of case 1 and case 2 in rough fractures. (**a**) Average height of sand dune; (**b**) Ratio of dune area to fracture area.

Table 3
Numerical simulation scheme.

Parameters	Value
Wall roughness	Smooth fracture, $D_f = 2.3$, 2.7
Inclined angle of secondary fracture, degree	0, 30, 60, 90
Approach angle of secondary fracture, degree	30, 60, 90, 120, 150
Injection rate, m/s	0.3, 0.5, 0.7
Proppant size, mm	0.6, 1
Fracturing fluid viscosity, mPa s	5, 10, 20
Injection position	Upper, middle and lower

5.2. Effect of fracture roughness

5.2.1. Single primary fracture

Two sets of single primary fractures with high roughness $D_f = 2.7$ and low roughness $D_f = 2.3$ were created to simulate proppant placement and migration, and one set of simulation was performed as a reference. The simulation results are shown in Fig. 8. The arrow directions in the figure are the directions of fluid flow and particle injection, which have the same meanings below. Intuitive observation shows that the rough wall has a significant effect on the distribution morphology of sand dune. In Fig. 9c, the non-uniformity of sand dune placement, i.e. the square error between the sand dune height and the average sand dune height is increased with the increase in roughness. The sand dunes within smooth fractures have a smooth continuous morphology, and those within the rough fracture have a dent morphology. The reason is illustrated in Fig. 10. The characteristics of concave-convex rough wall affect the fracturing fluid flow behavior and cause eddy in the flow near the wall. The increase in wall roughness causes stronger eddy within the fracture. Moreover, collision occurs between proppants and between proppants and fracture wall during proppant migration, and the increased roughness enhances collision, resulting in disordered proppant settlement and accumulation within rough fractures, which does not occur within in smooth fractures.

A large number of eddies caused by rough walls lead to more proppant suspension capacity and less proppant settlement, resulting in a decrease of 31.9% and 11.4% in the average height and length of sand dune (Fig. 9a and b). As the fracturing fluid is pumped, the suspended proppants are carried to the far-end and settle down or are migrated out of the fracture outlet, and the proppant volume left within the fracture decreases accordingly. As shown in Fig. 9d, the average height of the sand dune within the fracture with a roughness of $D_f = 2.7$ is only 63.8% of that within the smooth fracture. The ratio of dune area to fracture area decreases by 33%.

5.2.2. Complex fractures

Numerical simulation of proppant placement and migration within the complex fracture with same wall roughness as the single primary fracture was performed, as shown in Fig. 11.

The distribution morphology of sand dune and the unfilled degree (the ratio of the unfilled proppant area to the fracture area) in the near-wellbore area within the complex fracture is consistent with that in the single primary fracture, and the non-uniformity and unfilled degree in the near-wellbore area increases with increase in roughness. Proppants migrated within the rough and complex fracture mainly accumulate behind fracture nodes, forming large sand dune, which is significantly different from the phenomenon in the single primary fracture. Moreover, more proppants migrated within the rough fracture flow into the secondary fracture. As shown in Fig. 12, with the increase in roughness, the length and average height of sand dune within secondary and tertiary fractures increase gradually. The average sand dune height in the secondary fracture with a roughness of $D_f = 2.7$ is slightly lower due to that part of proppants flow out of fractures with limit length. This indicates the rough wall enhances proppant migration and cause proppant migration into the farther and deeper fracture zone.

5.3. Effect of inclined angle of branch fracture

Sahai (2012) and Wen et al. (2016) found that the natural fractures are possibly not perpendicular to the hydraulic fracture. The angle direction can be divided into inclined angle and approach angle. In order to investigate the effect of secondary fracture inclined angle on proppant migration and placement, numerical simulation was performed in the complex fracture models with secondary fractures connected to the 1/2 point of the primary fracture at inclined angles of 0°, 30°, 60° and 90°, and the results are shown in Fig. 13.

The secondary fractures mainly affect the sand dune distribution behind nodes at the primary fracture. As the inclined angle of the secondary fracture increases, the distributary effect of the secondary fracture decreases, and less proppants are carried by fracturing fluid to the secondary fracture, resulting in an increase in the sand dune height and length in the primary fracture. Fig. 14 shows that the maximum average height and length of sand dune are found in the primary fracture corresponding to the 90° inclined angle of the secondary fracture. Thus, the maximum ratio of dune area to fracture area occurs in primary fracture (Fig. 15) is 37%.

Comparatively, the inclined angle has a significant effect on proppant migration and placement within the secondary fracture. Proppants within the inclined fractures settle down under the wall support force, gravity and upward friction along the rough slope. The smaller incline causes the larger friction along the slope and

Table 4
Numerical parameters.

Parameters	Value	Parameters	Value
Proppant diameter, mm	0.8	Injection rate, m/s	0.4
Proppant density, kg/m^3	2500	Inlet opening	Full open
Fracturing fluid viscosity, Pa s	0.005	Roughness D_f	2.3
Fracturing fluid density, kg/m^3	1000	Fracture node morphology	Vertical
Proppant concentration, %	5	Fracture node location	1/2 of primary fracture length
Primary fracture size, mm	500 × 60 × 5	Secondary fracture size, mm	150 × 60 × 3
Number of primary fracture network	500 × 60 × 5 (Average)	Number of secondary fracture network	150 × 60 × 3 (Average)

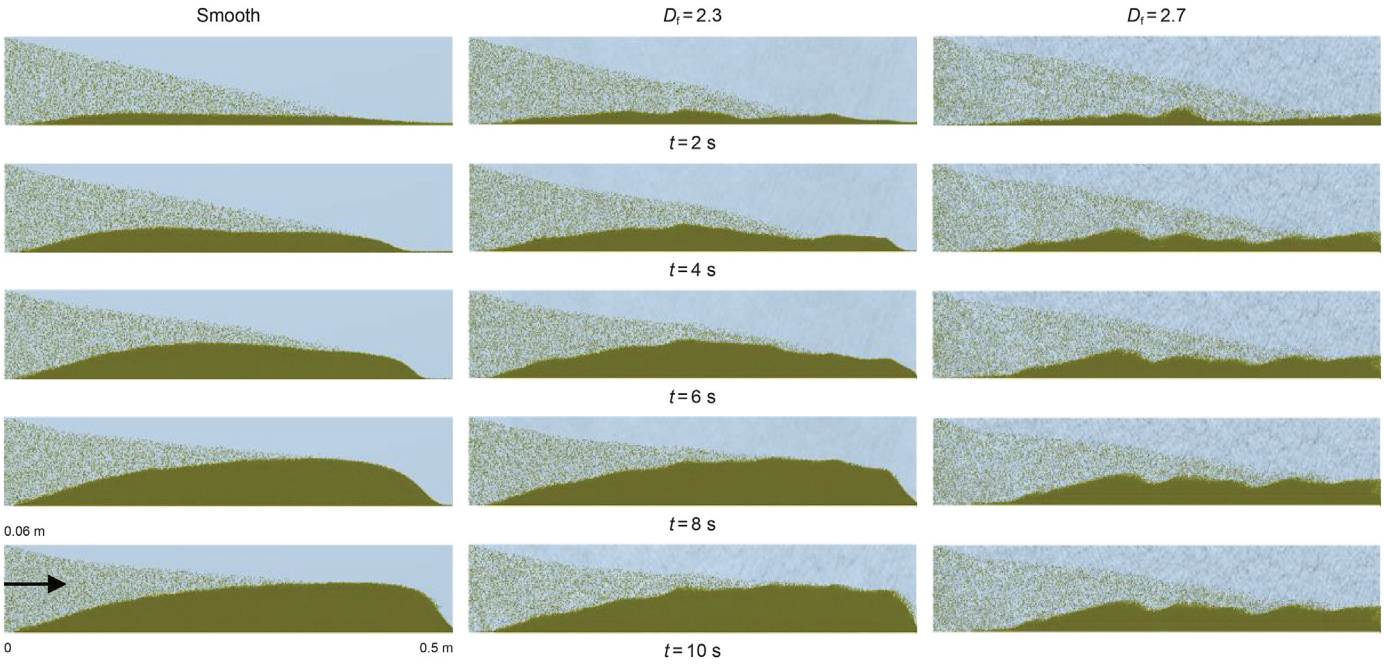

Fig. 8. Proppant distribution within a single primary fracture of different roughness at different time.

the weaker effect of gravity. Under the same kinetic energy, the proppants are migrated farther in the fracture with the smaller inclined angle, resulting in the larger proppant placement area. The proppants within the horizontal fracture at the inclined angle of 0° are subjected to the strongest friction and the gravity along the fracture width, resulting in much less settlement space, limited suspension, increasing settlement, and the maximum flow area within the horizontal fracture. The maximum average height and length of sand dune within the secondary fracture at an inclined angle of 0° leads to the highest ratio of dune area to fracture area up to 89%. With the increase in inclined angle, the proppants are subjected to less friction force and stronger gravity, more proppant fall into the secondary fracture and accumulate gradually, and the ratio of dune area to fracture area in the secondary fracture gradually decreases. When the inclined angle of secondary fracture increases to 90° (vertical), the ratio of dune area to fracture area within the secondary fracture is only 25%, which is minimum and decreases by 64% compared with that of the maximum sand dune area.

5.4. Effect of approach angle of branch fracture

The approach angle, i.e. the angle between the secondary fracture and the fluid flow direction within the primary fracture, is another factor affecting proppant migration and placement when the hydraulic fracture is not perpendicular to the natural fracture. Numerical simulation of proppant placement and migration within the secondary fractures connected to the 1/2 point of the primary fracture at angles of 30°, 60°, 90°, 120° and 150° was performed to study the effect of the approach angle, and the proppant distribution morphology was obtained, as shown in Fig. 16. The average height and length of sand dunes in the primary and secondary fractures is compared (Fig. 17). The ratio of dune area to fracture area in primary and secondary fractures at different approach angles is obtained (Fig. 18). The approach angle mainly affects the distribution morphology of the sand dune behind the node in the primary fracture. As the approach angle increases from 30° to 150°, the average height and length of the sand dune in the primary fracture increase gradually, and those in the secondary fracture decrease gradually. The proppants enter the secondary fracture through gravity and carrying of fracturing fluid. The flow direction in the secondary fracture at smaller approach angle is closer to that in the primary fracture, which leads to a reduction in the flow resistance and an increase in fluid distributary, and a large number of proppants are carried by the fracturing fluids to the secondary fracture. A limited number of proppants fall into the secondary fracture at high approach angle by gravity. The secondary fracture at an approach angle of 30° has the best filling effect, with ratio of dune area to fracture area is 34.3%. The ratio of dune area to fracture area in the secondary fracture at an approach angle of 150° is 20.8%, which decreases by 13.5%. Proppants not entering into the secondary fracture continue to be migrated and deposit within the primary fracture. The sand dune placement area is only 37.5% in the primary fracture connected to the secondary fracture at an approach angle of 30° and is 50%, which increases by 12.5%, when the approach angle is 150°.

5.5. Effect of injection rate

Injection rate, a key operation parameter, affects the particle migration behavior within fractures and the sand dune placement morphology (Kou et al., 2019). In order to investigate the effect of injection rate, simulation of proppant migration and placement within rough fractures was performed at an injection rate of 0.3, 0.5, and 0.7 m/s, respectively, in the complex fracture model with tertiary fractures were created, as shown in Fig. 19. According to Fig. 20, the injection rate increases from 0.3 to 0.7 m/s, the average sand dune height in the primary fracture decreases by 45%, and the sand dune length increases first and then decreases. Moreover, the fracturing fluid under the high injection rate carries more proppants into the secondary and tertiary fractures, where the sand dune length increases by 88% and 217%, respectively. An increase in injection rate leads to an increase in the energy for particle migration and an increase in its horizontal migration distance, and subsequent injection of fracturing fluid causes proppant settlement and accumulation in a long distance. According to Fig. 21, the

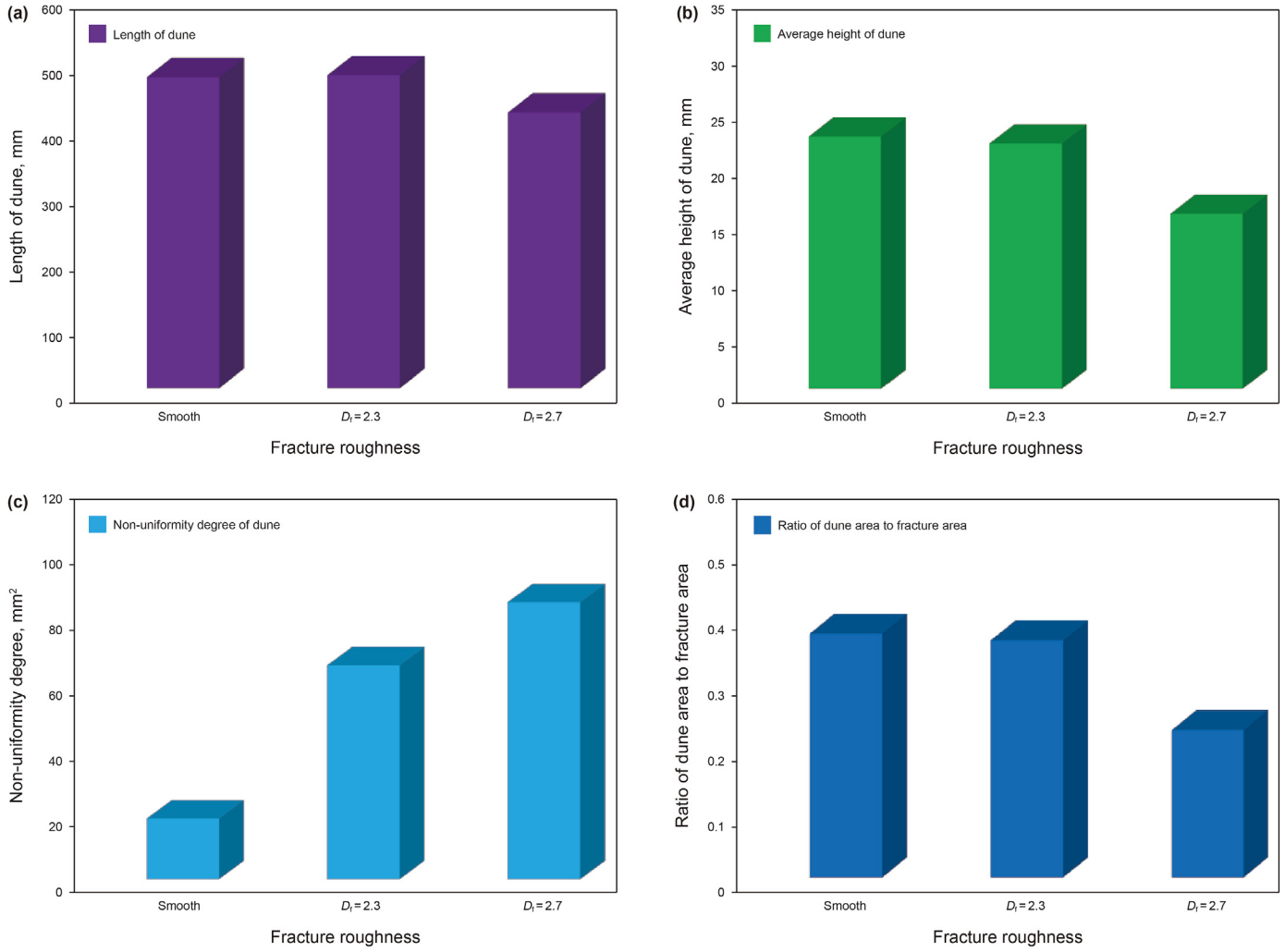

Fig. 9. Relationship between sand dune parameters and fracture roughness (t = 10 s). (**a**) Length of sand dune; (**b**) Average height of sand dune; (**c**) Degree of non-uniformity; (**d**) Ratio of dune area to fracture area.

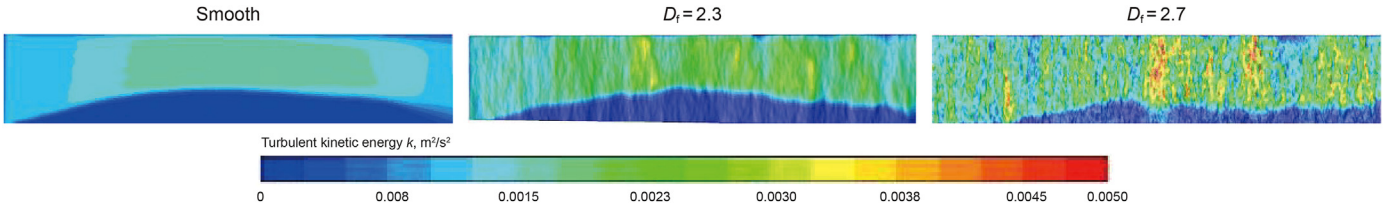

Fig. 10. Fluid turbulence within the fractures of different roughness (t = 6 s).

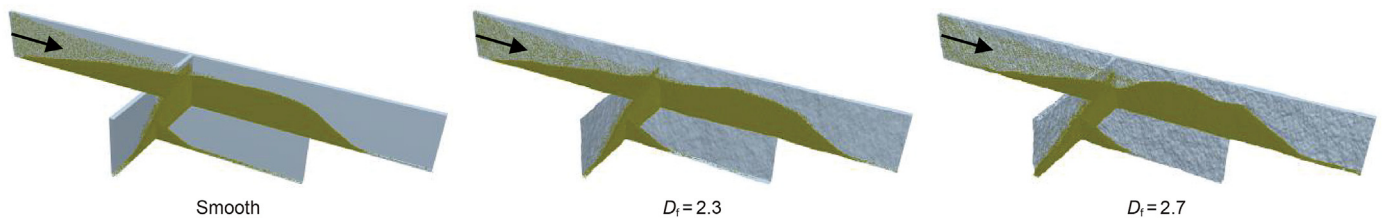

Fig. 11. Proppant distribution within complex fractures of different roughness.

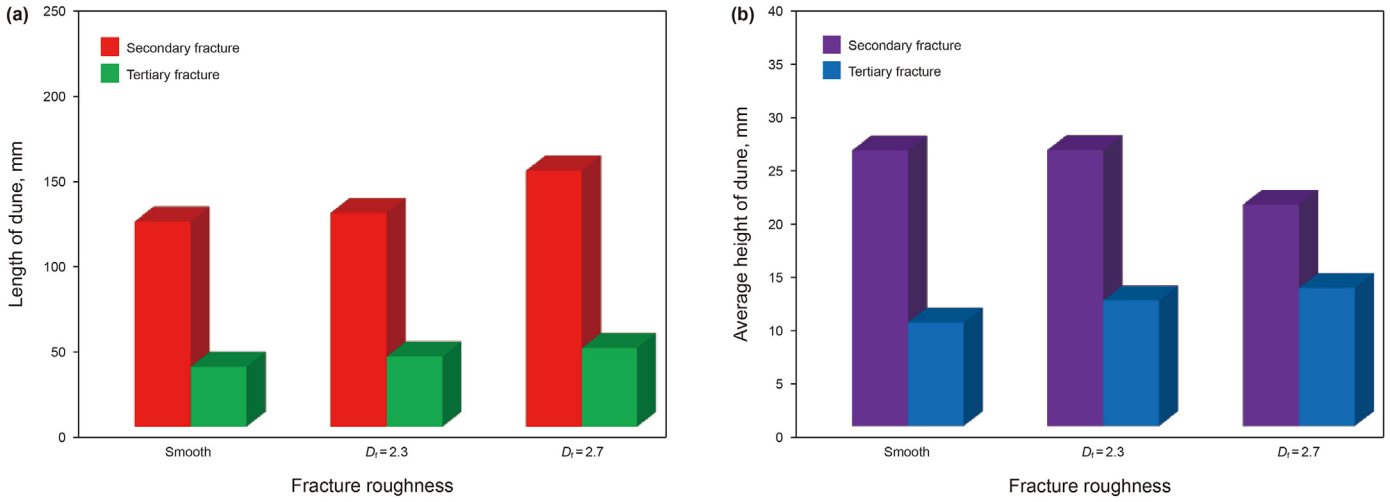

Fig. 12. Average height and length of sand dunes within fractures of different roughness.

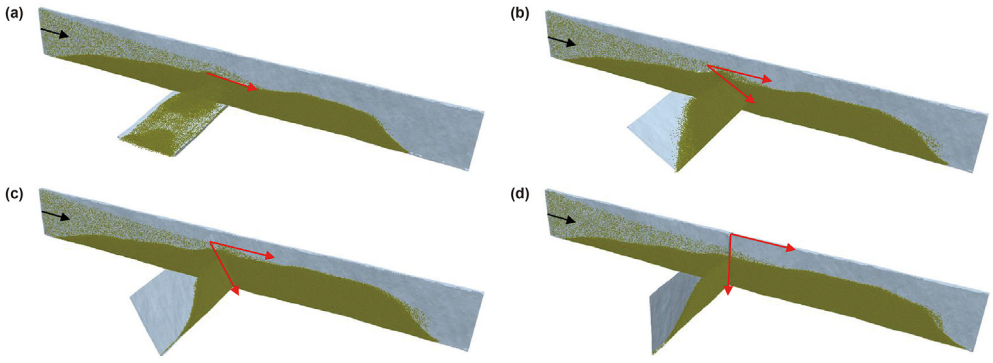

Fig. 13. Proppant distribution under different inclined angles of secondary fracture. (**a**) 0°; (**b**) 30°; (**c**) 60°; (**d**) 90°.

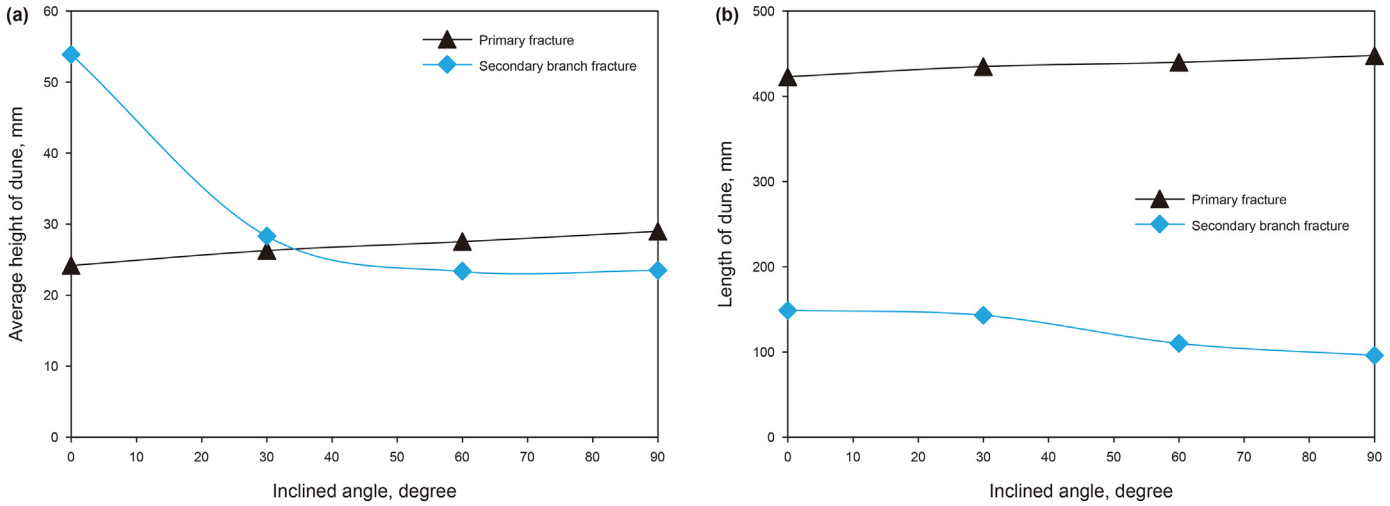

Fig. 14. Relationship between the average height and length of sand dune and the inclined angle.

injection rate of 0.3 and 0.7 m/s leads to a maximum of 42.9% and a minimum of 16.3%, which decreases by 26.6%, in the ratio of sand dune placement area in the primary fracture, and on the contrary, the ratio of sand dune area in secondary and tertiary fracture increases by 67% and 647%, respectively. An increase in injection rate contributes to proppant migration. Nevertheless, the unfilled degree in the near-wellbore area is increased dramatically, as shown in Fig. 22. The fracture opening is possibly closed under *in-situ* stress after fracturing. Thus, high injection rate is not conducive to filling of the near-wellbore fracture.

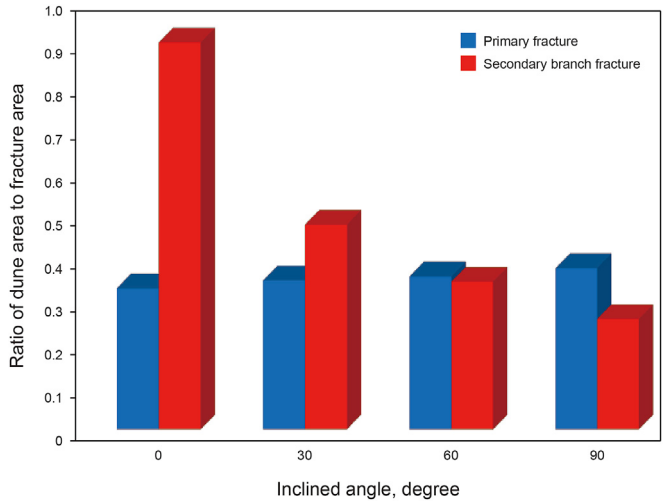

Fig. 15. Ratio of dune area to fracture area under different inclined angles of secondary fracture.

5.6. Effect of proppant size

Particle size is a key property of proppant and affects proppant migration and settlement within fractures. Simulation was performed with proppants with diameter of 1 mm and 0.6 mm, and the results are shown in Fig. 23, including the simulation results of injection of single-size particles in (a) and (b) and those of staged injection of dual-particle sizes in (c) and (d). According to Eq. (14), Stokes correlation of settlement velocity, the particle settlement velocity is proportional to the square of particle size, and the large size particles settle down rapidly. According to (a) and (b), the large size proppants accumulate into higher sand dunes and are migrated in a shorter distance, and the smaller size particle tend to be carried to far-end of fracture and deposit, forming longer sand dunes. The staged proppant injection causes obvious layering of sand dune. According to (c), the small proppants injected first form a long and short sand dune, and the large proppants injected later form a short and high sand dune above the previous sand dune. The particles of two sizes are not mixed. The proppant injection sequence in (d) is opposite to that in (c). The large particles injected first begin to settle down at the fracture inlet, forming a short and high sand dune. The smaller proppants injected later pass the lower sand dune of large particles and settle down at the back. As more proppants are injected, the sand dune more forward gradually. In this process, some particles at the top of sand dune of large particles are possibly swept by small particles, and proppant mixing occurs at the front of sand dune in (d).

$$\boldsymbol{V}_s = \frac{\boldsymbol{g}\left(\rho_p - \rho_f\right)d_p^2}{18\boldsymbol{\mu}_f} \tag{14}$$

where $\boldsymbol{V}_s$ is the proppant settlement velocity; $\boldsymbol{g}$ is the acceleration of gravity; ρ_p is the proppant density; ρ_f is the fluid density; d_p is the proppant diameter; $\boldsymbol{\mu}_f$ is the fluid viscosity.

Little proppants are migrated into the tertiary fracture in all four cases, and only the sand dune parameters in the primary and secondary fractures are analyzed. According to Fig. 24, the filling effect of the primary and secondary fractures by large size proppants are better than that by the small size proppants in the single size injection. It is necessary to perform staged injection to obtain better placement effect within the primary fracture, and the optimal way is to inject small size particles followed by large size particles, which increases the placement area by 13%–26%. Injection of large size proppants followed by small proppants results in an increase of 19%–25% in the placement area.

5.7. Effect of fracturing fluid viscosity

Viscosity is a key property of fracturing fluid and is used to characterize its sand-carrying capacity, and it has a significant effect on particle settlement and migration. Simulation with the fracturing fluid viscosity of 5, 10, and 20 mPa s was performed to obtain the effect of fracturing fluid viscosity on proppant placement and migration, as shown in Fig. 25. According to Eq. (14), the particle settlement velocity is inversely proportional to fluid viscosity, and particle settlement velocity decreases with the increase in fracturing fluid viscosity. Moreover, the increased fluid viscosity leads to an increase in the drag force on particles and enhances proppant migration. As shown in Fig. 26, more proppants carried by high viscosity fluid are migrated to and settle down in the

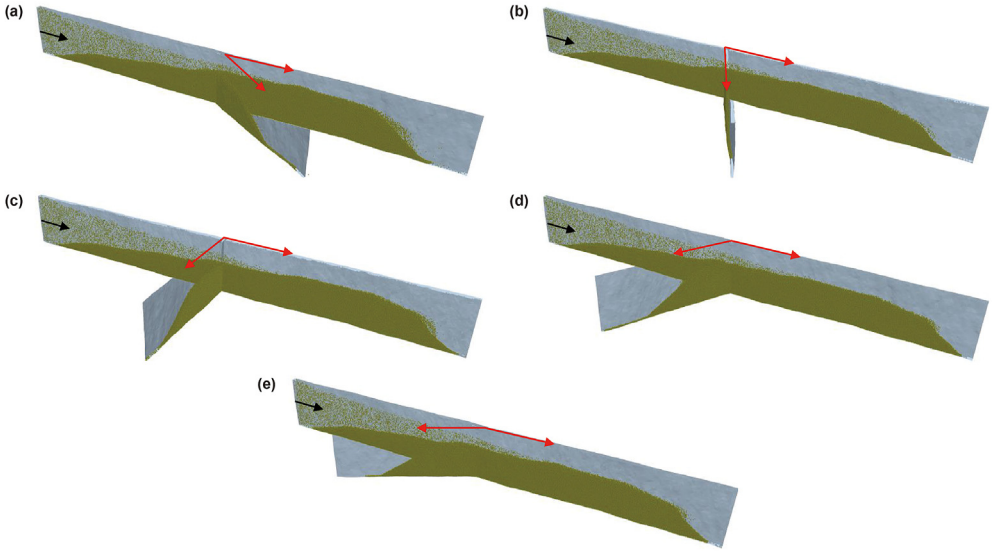

Fig. 16. Proppant distribution under different inclined angles of secondary fracture. (**a**) 30°; (**b**) 60°; (**c**) 90°; (**d**) 120°; (**e**) 120°.

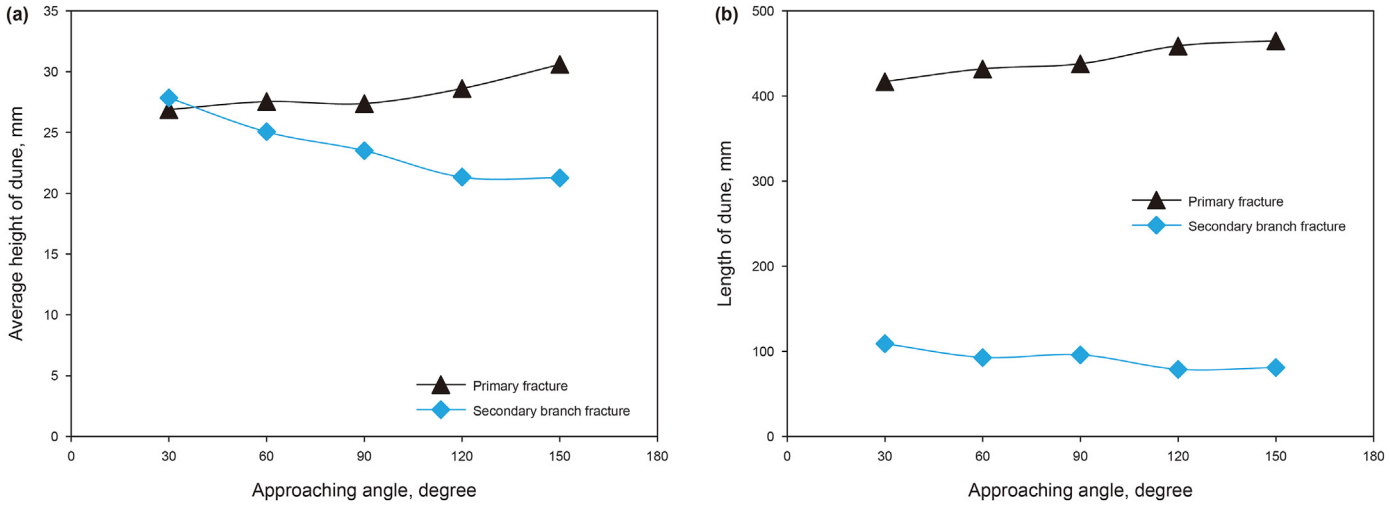

Fig. 17. Relationship between average height and length of sand dune and approach angle of secondary fracture.

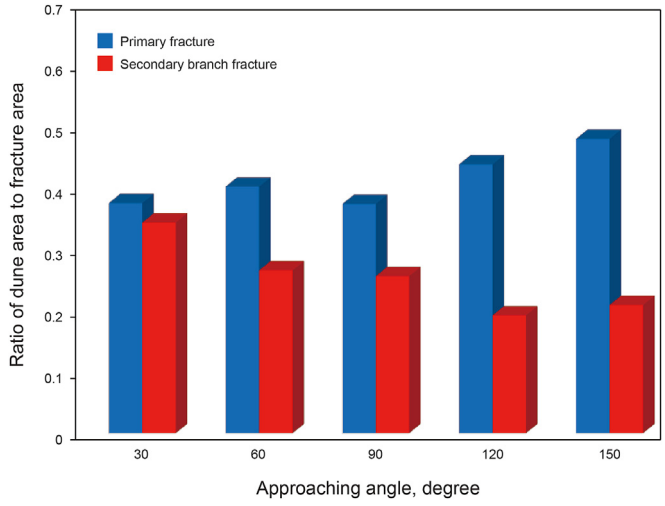

Fig. 18. Ratio of dune area to fracture area under different inclined angles of secondary fracture.

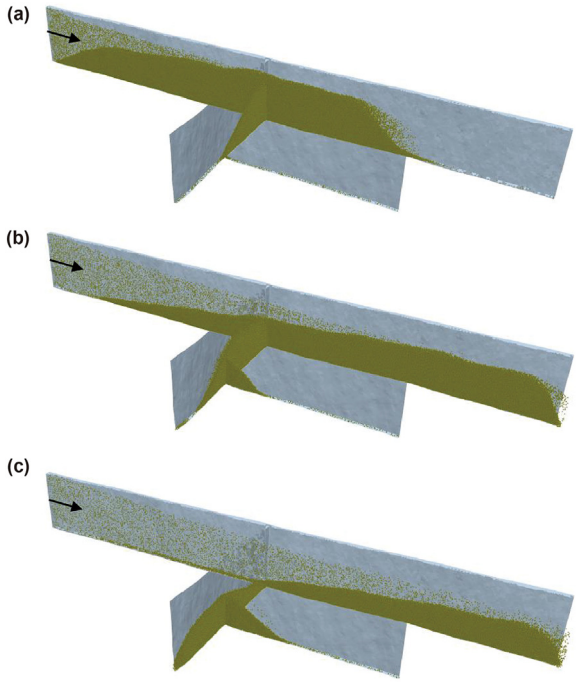

Fig. 19. Proppant distribution under different injection rates. (**a**) 0.3 m/s; (**b**) 0.5 m/s; (**c**) 0.7 m/s.

secondary fracture, resulting in an increase in the sand dune length and average height in the secondary fracture and a decrease in those in the primary fracture. An increase in the fracturing fluid viscosity from 5 to 20 mPa s leads to a reduction by 27% in the sand dune area in the primary fracture and an increase by 4% and 9% in the sand dune area in the secondary and tertiary fractures (see Fig. 27). According to Fig. 28, an increase in the fracturing fluid viscosity causes a significant increase in the unfilled degree in the near-wellbore area, and high injection rate and fracturing fluid viscosity are not conducive to filling of the fractures.

5.8. Effect of injection position

Considering that the contact area between fractures generated in horizontal fracturing and the wellbore is possibly very limited, it is simplified that the proppant together with sand-carrying fluid is injected into the fracture through a single perforation point. In order to investigate the effect of injection position on proppant migration and placement, the fracture inlet height was divided into four equal sections, where the upper, middle and lower round holes with diameter of 5 mm were set as fracturing fluid inlets. Simulation was performed by setting the injection rate as $v = 2$ m/s, and the simulation results are shown in Fig. 29, where colors from blue to red represents the sequence of proppant settlement.

For the proppants injected in the upper position, some start to settle down at the fracture inlet, and some are migrated farther before settlement. As more proppant are injected, more particles settle down, the rough fracture wall leads to the multi-dune morphology of the sand dune settle down early. Then, the concaves between the dunes are filled until the sand dune reaches the height of inlet, and the balance state is achieved.

Early injection in the middle creates a thin layer of sand dunes in the fracture entrance area similar to the upper injection, which is then eroded by high speed fracturing fluid and leaves behind a

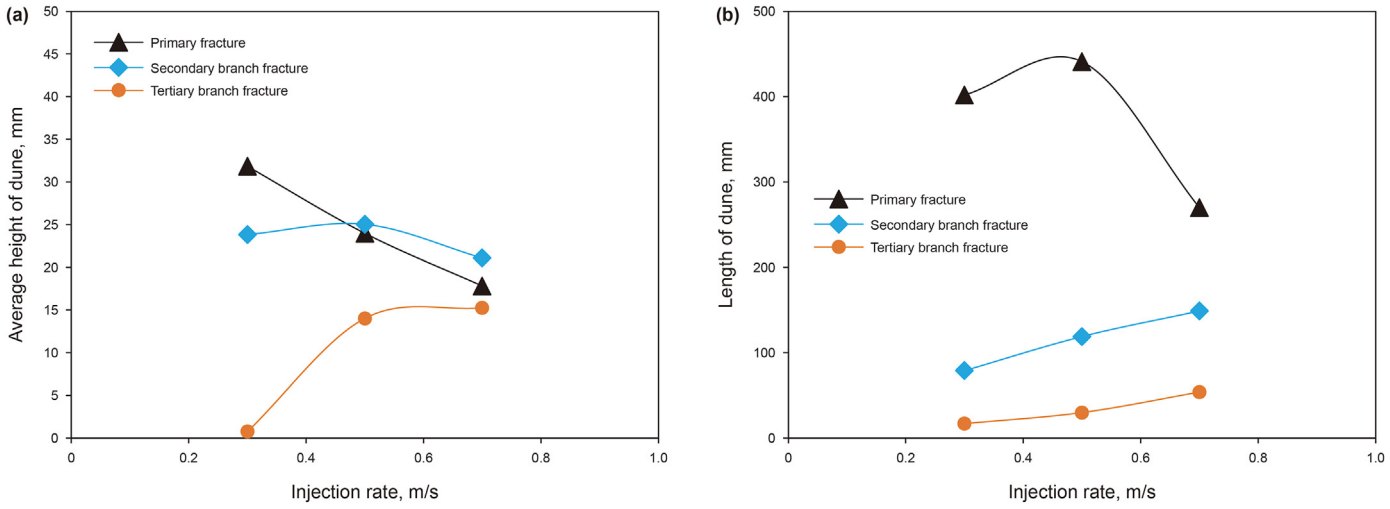

Fig. 20. Average height and length of sand dune vs. injection rate.

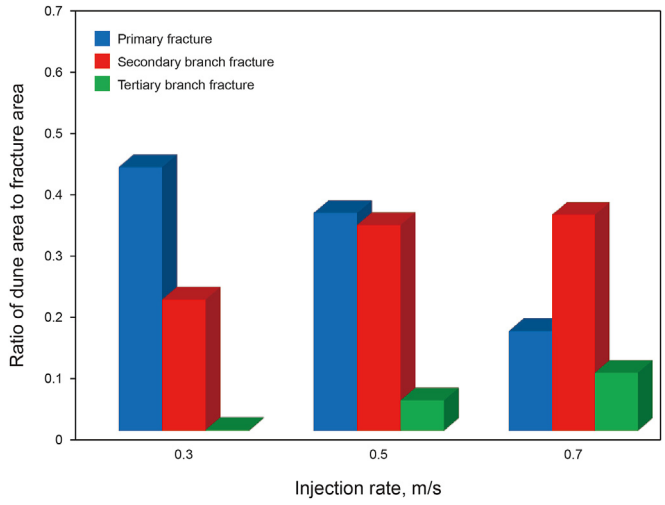

Fig. 21. Ratio of sand dune area to fracture area under different injection rates.

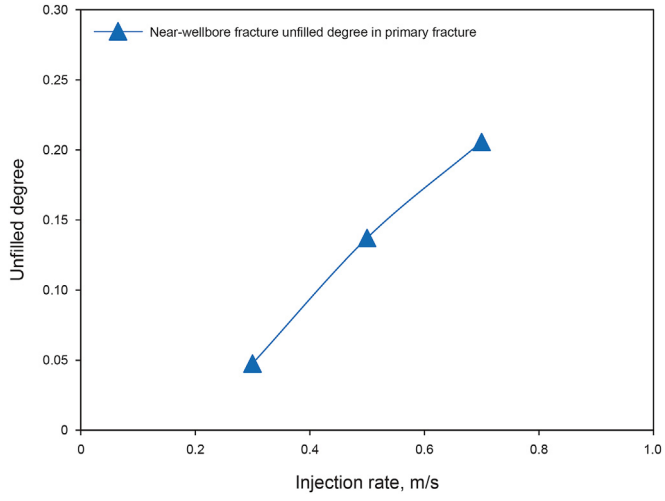

Fig. 22. Unfilled degree of primary fracture in the near-wellbore area vs. injection rate.

small sand dune. The proppant injected later migrates, accumulates, and grows forward. After lower injection, the proppant does not settle near the wellbore until it is transported far away and begins to settle due to gravity as kinetic energy dissipates. The sand dunes in the middle and lower injection shows the triangular morphology. As the sand dune grows continuously, its height is higher than the inlet, and it starts to block the flow field within the fracture, making the flow field turn upward. The particles injected subsequently are lifted up by the flow field and pass through sand dune. Then they roll down and settle down on top of the sand dune. The sand dune the reaches the balance status as injection goes on.

According to Fig. 30, the injection position has little effect on the sand dune placement area but has a significant effect on the unfilled degree in the near-wellbore area. The proppants injected in the upper position are migrated in a shorter distance and tend to settle down in the front and middle parts of the fractures, and non-proppant zone does not occur in the near-wellbore area. In contrast, the proppants injected in the middle position are migrated in a longest distance and tend to fill the middle and back parts of the fracture, creating the largest unfilled degree in the near-wellbore area. The proppants injected in the lower position mainly fill the middle part of the fracture, and the front and back parts are not effectively filled.

6. Conclusions and suggestions

In this paper, numerical simulation was performed through CFD-DEM coupling method to determine the effect of the fracture wall roughness, the inclined angle and approach angle of branch fracture, the injection rate, the proppant size, the fracturing fluid viscosity and the injection location on proppant migration and placement within the complex rough fracture. The conclusions are as follows.

(1) The proppant placement non-uniformity and proppant migration distance, and proppant volume filled in the far-end and the secondary branched fracture are enhanced within the rough fracture compared with those within smooth fractures, and the average height and area of dune are decreased.
(2) The inclination angle and approach angle of branch fracture have an effect on the sand dune morphology behind the primary fracture nodes and the branch fracture. The

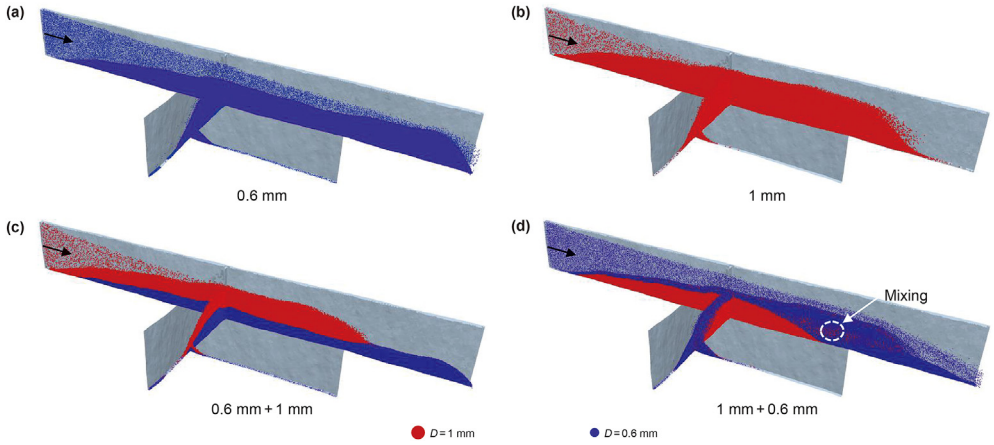

Fig. 23. Proppant distribution under different particle sizes. (**a**), (**b**) Single particle size injection; (**c**) Injection with 0.6 mm particle size in the first half of the simulation time, and 1 mm particle size in the last 1/2 of the simulation time; (**d**) The same as (**c**) on the contrary.

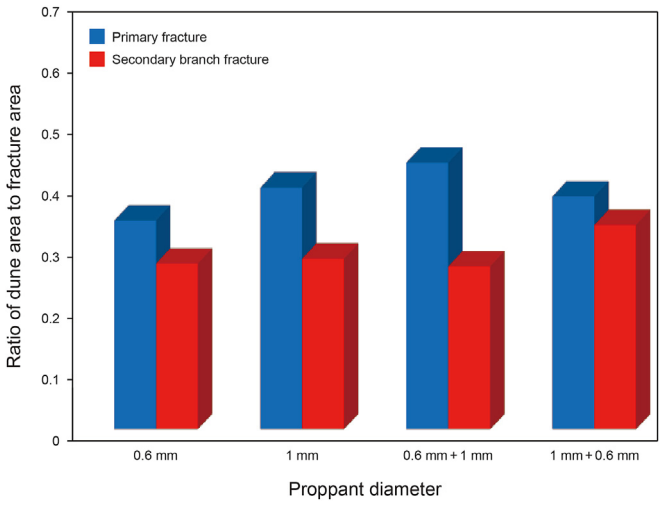

Fig. 24. Ratio of sand dune area to fracture area under different particle sizes.

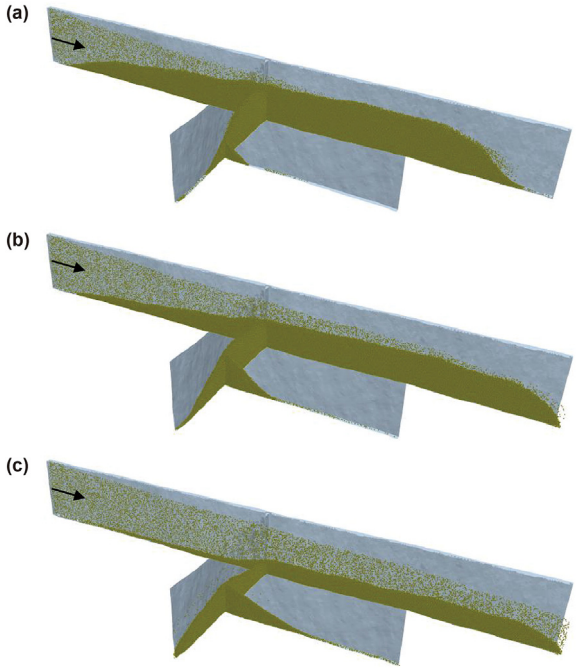

Fig. 25. Proppant distribution under different fracturing fluid viscosity. (**a**) 5 Pa s; (**b**) 10 Pa s; (**c**) 20 Pa s.

proppant placement area is larger in the inclined fracture than that in the vertical fracture. The proppant migrated to the branch fracture is increased within the fracture at low inclination angles (<60°) and low approach angles (<90°) of the branch fracture, and the sand dune behind the primary fracture node grows at high inclination angles (>60°) and high approach angles (>90°) of the branch fracture.

(3) The rise of injection rate and fracturing fluid viscosity causes more proppants migrate to far-end or secondary fractures. When the injection rate increased from 0.3 to 0.7 m/s, the proportion of sand dune near wellbore fractures decreased by 26.6%; when the fracturing fluid viscosity increased from 5 to 20 mPa s, the ratio of dune area to fracture area decreased by 27% accordingly. When the injection rate and fracturing fluid viscosity are too high, the unfilled degree in the near-well bore area increases rapidly.

(4) The large size enhances particle settlement, and the small size enhances particle transportation. The staged injection with small size proppants followed by large size proppants increases the proppant placement area in the primary fracture by 13%–26%, and that with large size proppants followed by small size proppants increases the proppant placement area by 19%–25%, which is due to that the latter method facilitates filling of the secondary branched fracture.

(5) The proppants injected in the upper position tend to settle down in the front and middle parts of the fractures, and non-proppant zone does not occur in the near-wellbore area. In contrast, the proppants injected in the middle position are migrated in a longest distance and tend to fill the middle and back parts of the fracture, creating the largest unfilled degree in the near-wellbore area. The proppants injected in the lower position mainly fill the middle part of the fracture, and the front and back parts are not effectively filled.

The results provide several suggestions for hydraulic fracturing treatments.

In rough fracture, the high injection rate and fracturing fluid viscosity and the middle injection lead to a significant increase in

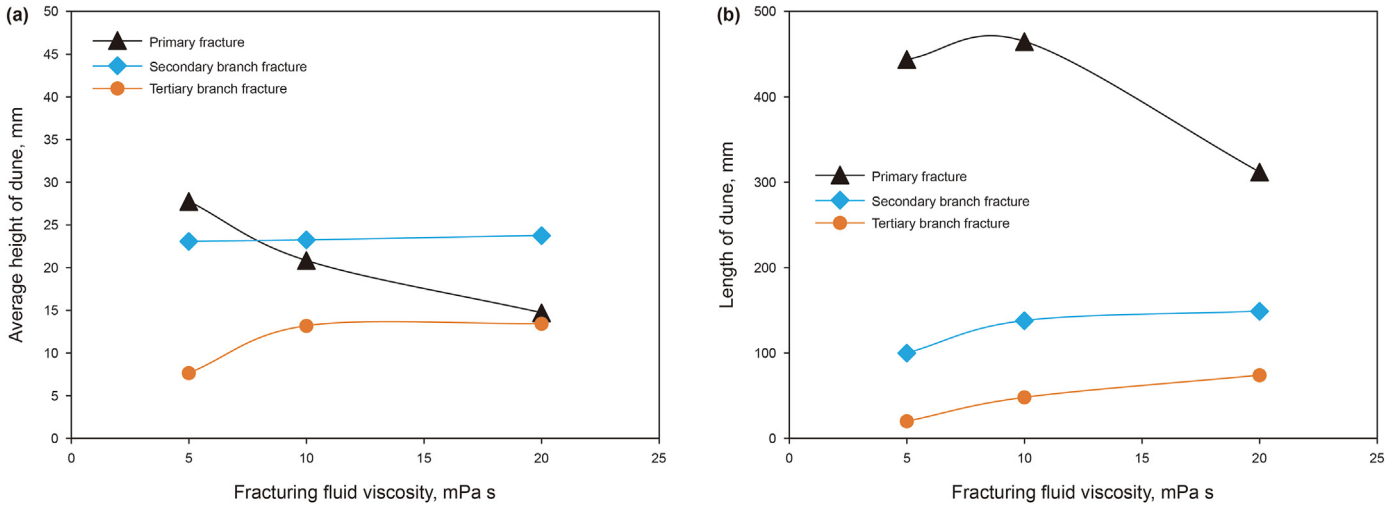

Fig. 26. Average height and length of sand dune vs. fracturing fluid viscosity.

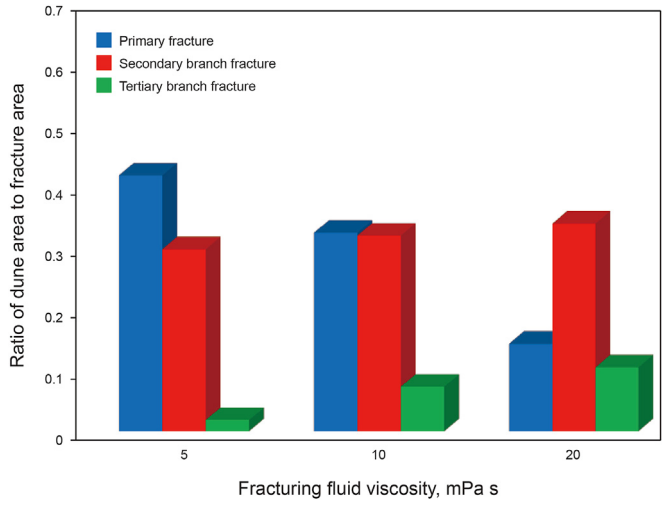

Fig. 27. Ratio of sand dune area to fracture area under different fracturing fluid viscosity.

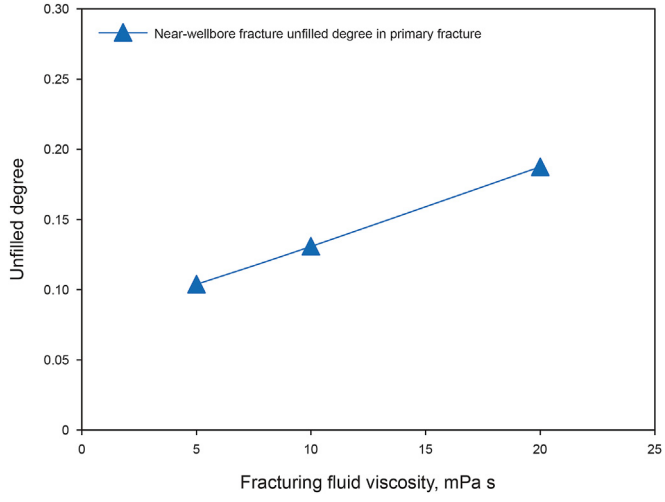

Fig. 28. Unfilled degree of primary fracture in the near-wellbore area vs. fracturing fluid viscosity.

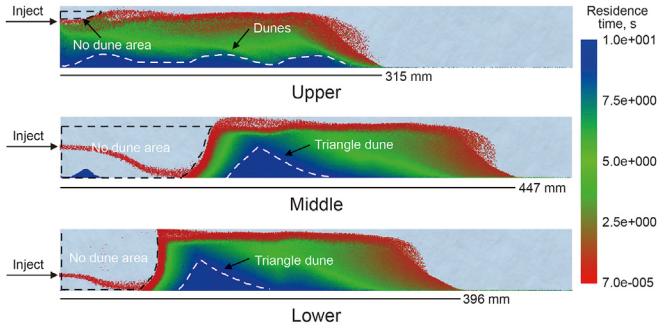

Fig. 29. Proppant distribution under different injection positions.

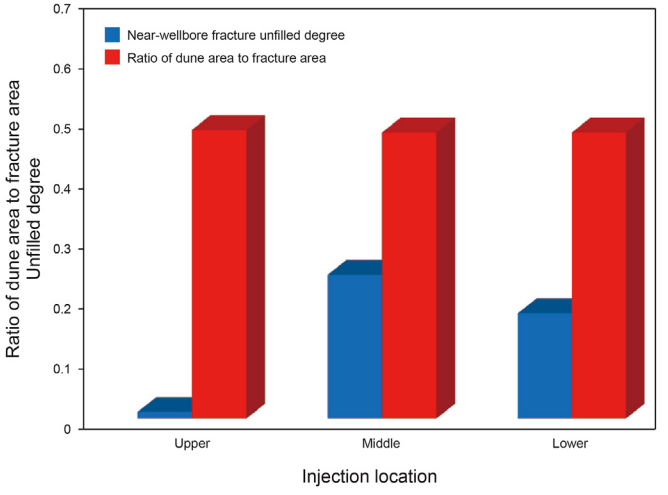

Fig. 30. Ratio of sand dune area to fracture area and unfilled degree in the near-wellbore area under different injection positions.

the proppant migration distance, the tendency of filling of fracture in the far end, and the low unfilled degree and no-proppant zone in the near-wellbore area. The large particle size and low injection rate and viscosity provides a supplement to filling of the no-proppant area and promotes the filling effect of fracture.

The difficulty of getting proppant into a branch fracture

increases with the complexity of the fracture network. The filling effect of complex fracture can be enhanced by promoting filling of secondary branch fracture and the far-end fracture through high injection rate and fracturing fluid viscosity and small particle size and achieving filling of the near-well bore fracture through large particle size and low injection rate and fracturing fluid viscosity.

Acknowledgements

The authors would like to acknowledge the financial support of the National Natural Science Foundation of China (Grant No. 52074332), and express their gratitude to project ZR2020YQ36 supported by Shandong Provincial Science Fund for Excellent Young Scholars.

References

Abubakar, I., Moaz, H., Khaled, A.A., Murtada, S.A., Mohamed, M., 2021. A comprehensive review of proppant transport in fractured reservoirs: experimental, numerical, and field aspects. J. Nat. Gas Sci. Eng. 88, 103832. https://doi.org/10.1016/j.jngse.2021.103832.

Ainni, S.R., Rohani, M.Z., Noor, F.A.B., Nur, H.O., 2021. Recent progress on proppant laboratory testing method: characterisation, conductivity, transportation, and erosivity. J. Petrol. Sci. Eng. 205, 108871. https://doi.org/10.1016/j.petrol.2021.108871.

Alotaibi, M.A., Miskimins, J.L., 2017. Slickwater proppant transport in hydraulic fractures: new experimental findings and scalable correlation. SPE Prod. Oper. 33, 164–178. https://doi.org/10.2118/174828-PA.

Ba Geri, M., Imqam, A., Mohammed, S., 2019. Investigate proppant transport with varying perforation density and its impact on proppant dune development inside hydraulic fractures. In: SPE Middle East Oil and Gas Show and Conference. https://doi.org/10.2118/195018-MS.

Babadagli, T., Develi, K., 2003. Fractal characteristics of rocks fractured under tension. Theor. Appl. Fract. Mech. 39 (1), 73–88. https://doi.org/10.1016/S0167-8442(02)00139-8.

Bandara, K., Ranjith, P.G., Rathnaweera, T.D., 2020. Laboratory-scale study on proppant behaviour in unconventional oil and gas reservoir formations. J. Nat. Gas Sci. Eng. 78, 103329. https://doi.org/10.1016/j.jngse.2020.103329.

Beatriz, R.B., Chen, B., Li, C.F., 2021. A review on proppant transport modelling. J. Petrol. Sci. Eng. 204, 108753. https://doi.org/10.1016/j.petrol.2021.108753.

Bokane, A., Jain, S., Deshpande, Y., Freddy, C., 2013. Transport and distribution of proppant in multistage fractured horizontal wells: a CFD simulation approach. In: SPE Annual Technical Conference and Exhibition. https://doi.org/10.2118/166096-MS.

Deng, S.C., Li, H.B., Ma, G.W., Huang, H., Li, X., 2014. Simulation of shale–proppant interaction in hydraulic fracturing by the discrete element method. Int. J. Rock Mech. Min. Sci. 70, 219–228. https://doi.org/10.1016/j.ijrmms.2014.04.011, 10.16285/j.rsm.2016.05.036.

Gadde, P.B., Liu, Y.J., Norman, J., Bonnecaze, R., Sharma, M.M., 2004. Modeling proppant settling in water-fracs. In: SPE Annual Technical Conference and Exhibition. https://doi.org/10.2118/89875-MS.

Gong, D.G., Qu, Z.Q., Li, J.X., Qu, G.Z., Cao, Y.C., Guo, T.K., 2016. Extended finite element simulation of hydraulic fracture based on ABAQUS platform. Rock Soil Mech. 37 (5), 1512–1520.

Gong, F.C., Guo, T.K., Sun, W., Li, Z.M., Yang, B., Chen, Y.M., Qu, Z.Q., 2020. Evaluation of geothermal energy extraction in Enhanced Geothermal System (EGS) with multiple fracturing horizontal wells (MFHW). Renew. Energy 151, 1339–1351. https://doi.org/10.1016/j.renene.2019.11.134.

Gong, Y.W., Mohamed, M., Ilham, E., Hari, V., 2020. Proppant placement in complex fracture geometries: a computational fluid dynamics study. J. Nat. Gas Sci. Eng. 79, 103295. https://doi.org/10.1016/j.jngse.2020.103295.

Guo, T.K., Qu, Z.Q., Li, M.Z., Chen, D.C., Dong, C.Y., Wang, W.Y., Qi, N., 2018. Development of virtual simulation device for proppant migration and placement in large complex fractures. Laboratory Research and Exploration 37 (10), 248–252.

Guo, T.K., Li, Y.C., Ding, Y., Qu, Z.Q., Gai, N.C., Rui, Z.H., 2017. Evaluating of acid fracturing treatment in shale formation. Energy Fuel. 31 (10), 10479–10489. https://doi.org/10.1021/acs.energyfuels.7b01398.

Guo, T.K., Tang, S.J., Sun, J., Gong, F.C., Liu, X.Q., Qu, Z.Q., Zhang, W., 2020. A coupled thermal-hydraulic-mechanical modeling and evaluation of geothermal extraction in the enhanced geothermal system based on analytic hierarchy process and fuzzy comprehensive evaluation. Appl. Energy 258, 113981. https://doi.org/10.1016/j.apenergy.2019.113981.

Guo, T.K., Wang, X.Z., Li, Z., Gong, F.C., Lin, Q., Qu, Z.Q., Lv, W., Tian, Q.Z., Xie, Z.S., 2019. Numerical simulation study on fracture propagation of zipper and synchronous fracturing in hydrogen energy development. Int. J. Hydrogen Energy 44 (11), 5270–5285. https://doi.org/10.1016/j.ijhydene.2018.08.072.

Kou, R., Moridis, G.J., Blasingame, T.A., 2018. Analysis and modeling of proppant transport in inclined hydraulic fractures. In: SPE Hydraulic Fracturing Technology Conference and Exhibition. https://doi.org/10.2118/189856-MS.

Kou, Rui, Moridis, George, Thomas, B., 2019. Bridging criteria and distribution correlation for proppant transport in primary and secondary fracture. In: SPE Hydraulic Fracturing Technology Conference and Exhibition. https://doi.org/10.2118/194319-MS.

Liu, X.Q., Qu, Z.Q., Guo, T.K., Tian, Q.Z., Lv, W., Xie, Z.S., Chu, C.B., 2019. An innovative technology of directional propagation of hydraulic fracture guided by radial holes in fossil hydrogen energy development. Int. J. Hydrogen Energy 44 (11), 5286–5302. https://doi.org/10.1016/j.ijhydene.2018.07.189.

Lu, C., Ma, L., Li, Z., Huang, F., Huang, C., Yuan, H., Tang, Z., Guo, J., 2020. A novel hydraulic fracturing method based on the coupled cfd-dem numerical simulation study. Appl. Sci. 10 (9), 3027. https://doi.org/10.3390/app10093027.

Raimbay, A., Babadagli, T., Kuru, E., Develi, K., 2017. Effect of fracture roughness, shear displacement, fluid type, and proppant on the conductivity of a single fracture: a visual and quantitative analysis. SPE Reservoir Eval. Eng. 20, 446–470. https://doi.org/10.2118/171577-PA.

Sahai, R., 2012. Laboratory Evaluation of Proppant Transport in Complex Fracture Systems. MS Thesis. Colorado School of Mines, Golden, Colorado.

Sahai, R., Miskimins, Jennifer, L., Karen, E.O., 2014. Laboratory results of proppant transport in complex fracture systems. In: SPE Hydraulic Fracturing Technology Conference. https://doi.org/10.2118/168579-MS.

Sahai, R., Moghanloo, R.G., 2019. Proppant transport in complex fracture networks – a review. J. Petrol. Sci. Eng. 182, 106199. https://doi.org/10.1016/j.petrol.2019.106199.

Scott, B., Bryan, W.K., Brent, E.S., 2016. Numerical modeling of the effects of roughness on flow and eddy formation in fractures. J. Rock Mech. Geotech. Eng. 9 (1), 105–115. https://doi.org/10.1016/j.jrmge.2016.08.004.

Siddhamshetty, P., Mao, S.W., Wu, K., Joseph, S.K., 2020. Multi-size proppant pumping schedule of hydraulic fracturing: application to a MP-PIC model of unconventional reservoir for enhanced gas production. Processes 8 (5), 570. https://doi.org/10.3390/pr8050570.

Song, Y., Dahi, T.A., 2020. Numerical simulation of proppant placement in scaled fracture networks. J. Energy Resour. Technol. 143 (4), 043004. https://doi.org/10.1115/1.4048306.

Steven, R.O., Evgeny, I., Paul, W.J., Glover, 2006. Fluid flow through rough fractures in rocks. II: a new matching model for rough rock fractures. Earth Planet Sci. Lett. 241 (3–4), 454–465. https://doi.org/10.1016/j.epsl.2005.11.041.

Tong, S.Y., Mohanty, K.K., 2016. Proppant transport study in fractures with intersections. Fuel 181, 463–477. https://doi.org/10.1016/j.fuel.2016.04.144. ISSN 0016-2361.

Troy, C., Li, Y.C., Wu, K., 2020. Comprehensive experimental study of proppant transport in an inclined fracture. J. Petrol. Sci. Eng. 184, 106523. https://doi.org/10.1016/j.petrol.2019.10652.

Tsai, K., Fonseca, E.R., Degaleesan, S., Lake, E., 2012. Advanced computational modeling of proppant settling in water fractures for shale gas production. In: SPE Hydraulic Fracturing Technology Conference. https://doi.org/10.2118/151607-PA.

Wang, X.Y., Yao, J., Gong, L., Sun, H., Yang, Y.F., Zhang, L., Li, Y., Liu, W.C., 2019. Numerical simulations of proppant deposition and transport characteristics in hydraulic fractures and fracture networks. J. Petrol. Sci. Eng. 183, 106401. https://doi.org/10.1016/j.petrol.2019.106401.

Wen, C.Y., Yu, Y.H., 1966. Mechanics of fluidization. Chem. Eng. Prog. Symp. Ser. 62, 100–111.

Wen, Q.Z., Wang, S.T., Duan, X.F., Li, Y., Wang, F., Jin, X.C., 2016. Experimental investigation of proppant settling in complex hydraulic-natural fracture systems in shale reservoirs. J. Nat. Gas Sci. Eng. 33, 70–80. https://doi.org/10.1016/j.jngse.2016.05.010.

Wu, C.H., Sharma, M.M., 2016. Effect of perforation geometry and orientation on proppant placement in perforation clusters in a horizontal well. In: SPE Hydraulic Fracturing Technology Conference. https://doi.org/10.2118/179117-MS.

Yatin, S., Sheikh, Z.I., Mamdud, H., 2019. A new CFD approach for proppant transport in unconventional hydraulic fractures. J. Nat. Gas Sci. Eng. 70, 102951. https://doi.org/10.1016/j.jngse.2019.102951.

Zeng, J.S., Li, H., Zhang, D.X., 2016. Numerical simulation of proppant transport in hydraulic fracture with the upscaling CFD-DEM method. J. Nat. Gas Sci. Eng. 33, 264–277. https://doi.org/10.1016/j.jngse.2016.05.030.

Zeng, J.S., Li, H., Zhang, D.X., 2019. Numerical simulation of proppant transport in propagating fractures with the multi-phase particle-in-cell method. Fuel 245, 316–335. https://doi.org/10.1016/j.fuel.2019.02.056.

Zhang, G.D., Li, M.Z., Marte, G., 2017. Numerical simulation of proppant distribution in hydraulic fractures in horizontal wells. J. Nat. Gas Sci. Eng. 48, 157–168. https://doi.org/10.1016/j.jngse.2016.10.043.